Cement and Concrete Research 39 (2009) 701–715

Contents lists available at ScienceDirect

Cement and Concrete Research

journal homepage: http://ees.elsevier.com/CEMCON/default.asp

Application of nanoindentation testing to study of the interfacial transition zone in steel fiber reinforced mortar

Xiao Hui Wang [a,*], Stefan Jacobsen [b], Jian Ying He [b], Zhi Liang Zhang [b], Siaw Foon Lee [b], Hilde Lea Lein [c]

[a] Department of Civil Engineering, Shanghai Jiaotong University, Shanghai 200240, China
[b] Department of Structural Engineering, Faculty of Engineering Science and Technology, Norwegian University of Science and Technology (NTNU), 7491 Trondheim, Norway
[c] Department of Materials Science and Engineering, Faculty of Engineering Science and Technology, Norwegian University of Science and Technology (NTNU), 7491 Trondheim, Norway

ARTICLE INFO

Article history:
Received 14 August 2008
Accepted 13 May 2009

Keywords:
Nanoindentation
Scanning Electron Microscopy (SEM)
Interfacial transition zone (ITZ)
Elastic modulus and hardness
Steel fiber reinforced mortar

ABSTRACT

The characteristics of the profiles of elastic modulus and hardness of the steel fiber–matrix and fiber–matrix–aggregate interfacial zones in steel fiber reinforced mortars have been investigated by using nanoindentation and Scanning Electron Microscopy (SEM), where two sets of parameters, i.e. water/binder ratio and content of silica fume were considered. Different interfacial bond conditions in the interfacial transition zones (ITZ) are discussed. For sample without silica fume, efficient interfacial bonds across the steel fiber–matrix and fiber–matrix–aggregate interfaces are shown in low water/binder ratio mortar; while in high water/binder ratio mortar, due to the discontinuous bleeding voids underneath the fiber, the fiber–matrix bond is not very good. On the other hand, for sample with silica fume, the addition of 10% silica fume leads to no distinct presence of weak ITZ in the steel fiber–matrix interface; but the effect of the silica fume on the steel fiber–matrix–aggregate interfacial zone is not obvious due to voids in the vicinity of steel fiber.

1. Introduction

Fiber reinforced mortar is a composite structure at a microscopic scale. Its properties rely on the matrix, aggregate, fiber and the interfacial transition zone (ITZ) between the two. The transition area consists of a loose unit of hydrates of the neighboring cement grains. It consolidates with the progressing hydration and reaches in its "final phase" a porosity of about 50% [1]. The origin of the ITZ mainly lies in the so called "wall" effect of packing of cement grains against the relatively flat aggregate surface [2] or fiber, or steel surface, micro-bleeding effect which results in the accumulation of water under the aggregate particles and the flocculation effect of the small cement grains [3].

Due to the way it is formed the ITZ is not a definite zone, but a region of transition. Its effective thickness varies with the microstructural feature being studied and during the course of hydration [2]. The typical width of the ITZ between the aggregate and matrix is 50 μm; however, different researchers obtained different thicknesses of ITZ from their tests. For instance, the thickness of the transition zone between the aggregate and matrix ranged from 10 μm to about 30 μm [1]; Ollivier et al. [3] argued that there was only thickness of 15 μm to 20 μm around the aggregates, just equaling to the mean diameter of the cement grains. For the fiber–mortar interface, where amorphous cast iron fibers were used, fiber–matrix debonding generally occurred at some distance – about 5 μm – from the fiber surface where the porous zone was the weakest [4]. Although the size of the ITZ varied with different fiber type and fiber size as well as matrix details, most observations suggested a relatively large porous and weak layer on the order of 40 μm to 70 μm thickness [5]. For the ITZ around steel reinforcement, it was shown that the minimum micro-mechanical properties occurred at 10 ± 30 μm from the actual steel interface [6].

In the study of ITZ, a key question is to what extent the existence of ITZ has any practical influences on the engineering properties of cementitious materials, or it is just a peculiarity of academic interest [7]. There are two contrary opinions about this problem: some researchers argued that the ITZ is the weakest link between the cement paste and the aggregate, so it has a significant role in determining the properties of all cementitious composites [8–10]; however, Diamond and Huang [11] pointed out, that there is no reason to assume the significant negative effects of ITZ on permeance or mechanical properties of concrete, even for concrete with a water/binder ratio of 0.5. The reason for lack of conclusive evidences provided by various experimental researches carried out to the ITZ mainly lies in the limited sensitivity of the experimental technique or inappropriate methods yielding biased information [12]. In order to resolve this issue two committees were set up by RILEM and the conclusion are as follows [7]: 1) the ITZ should be viewed as a system property which is dependent on the overall composition and the method of fabrication of the cement composite; 2) the properties of the ITZ may have a moderate influence on the mechanical properties of concrete but not a drastic one; 3) the ITZ may have a drastic effect on the mechanical

* Corresponding author. Department of Civil Engineering, Shanghai Jiaotong University, Shanghai 200240, China. Tel.: +86 13167078307 or +86 47 73 597155.
E-mail address: w_xiaoh@163.com (X.H. Wang).

0008-8846/$ – see front matter
doi:10.1016/j.cemconres.2009.05.002

Table 1
Particle size and density of the steel fiber reinforced compounds.

Material	Particle size (μm)	Density (kg/m^3)
Anlegg cement	<30 μm: 80.1% and >90 μm:0.5%	3120
Silica fume	Retained on 45 μm sieve<1.5%	2200
Limestone powder	<30 μm: 64.3% and >90 μm: 5.6%	2730
Sand 0–4 mm	<125 μm: 6.1% and <4000 μm: 98.9%	2650
Sand 0–2 mm	<125 μm: 23.6% and <2000 μm: 91.8%	2650
Steel fiber	160 (diameter)	7800
Glenium 151	–	1030
Water	–	1000

properties of fiber reinforced cement composites and on their long term properties.

During the last decades, a lot of research works have been carried out to study the influence of various factors on ITZ between aggregate and paste. The ITZ between the fiber and matrix in fiber reinforced cement based composites was also studied due to its drastic effect on the mechanical and durability properties. The ITZ between the fiber and matrix was affected by the water/binder (w/b) ratio [13], age [14] and sand content [15]. Mineral admixtures such as silica fume [4,13,16] and fly ash [17] were also introduced to improve the quality of the fiber–matrix interfacial zone.

The morphological characteristic of the microstructure of ITZ is primarily characterized via electron microscopy. Throughout those researches, Scanning Electron Microscopy (SEM) [10,11], Environmental Scanning Electron Microscopy (ESEM) [13] and Transmission Electron Microscopy (TEM) [18] have been extensively used. In order to investigate and quantify microstructural gradients across the ITZ, backscattered electron imaging and energy dispersive X-ray map [2,19,20] have been also used. However, for the above mentioned microscopical techniques, only two dimensional sections of a three-dimensional microstructure can be observed [19].

For the purpose of developing test methods that can be used to determine the mechanical characteristics of microsize zones in various cement based composites, in locations that exhibit microstructural gradients, microhardness or microindentation testing was used to characterize gradients in mechanical properties to understand the influence of the interfacial transition zone [6,21–25]. Due to the limitations of microindentation, such as larger indent comparing with the thickness of ITZ [26], a new method – which has been already used for many other materials [27] – nanoindentation, began to be used in the cementitious composites. Since the cementitious materials exhibit heterogeneous features from the nano-scale to the macroscopic scale, by using the nanoindentation technique, better representation of this heterogeneity at multiple length scales, to ultimately identify the scale where physical chemistry meets mechanics can be obtained [28]. Till now, nanoindentation was widely used to measure elastic modulus and hardness of cement paste cured at different conditions [29–35]. Only few research works were focused on the *studying* of the ITZ between a rigid inclusion and matrix [36–38].

In the present paper, three types of steel fiber reinforced mortars were prepared. Good grinding and polishing procedures were finally determined for the nanoindentation test after several trial procedures had been made. Atomic Force Microscope (AFM) study was carried out to measure the surface roughness. Berkovich indenter was used to investigate the steel fiber–matrix interface and fiber–matrix–aggregate interface differences. Then, the indented areas were studied by Scanning Electron Microscopy (SEM). Influence of the water/binder ratio and silica fume on the characteristics of the profiles of the elastic modulus and hardness of the interfacial transition zones and the corresponding interfacial bond conditions was investigated.

2. Materials and methods

2.1. Materials and proportions of mixes used

The mortar mixes were prepared with cement, sands 0–4 mm and 0–2 mm, water, steel fiber, limestone powder and/or silica fume. Norcem Anlegg cement which is an ordinary Portland cement was used. Silica fume (Elkem Microsilica grade 940-U) in powder form with the content of SiO_2 larger than 90% was used. The limestone powder, used as a filler, has a fineness of 64.3% <30 μm. Sands 0–4 mm and 0–2 mm have fineness modulus of 2.37 and 1.51, respectively. Glenium 151 was incorporated in all mixes as a superplasticizer, having 15% solids content. Straight high carbon steel fiber OL13/.16 has a length of 13 mm and a diameter of 0.16 mm. The detailed particle sizes and densities of all the materials are summarized in Table 1.

Two water/binder ratios of 0.3 and 0.5 were adopted and two different contents of silica fume (0% and 10%) were considered to prepare steel fiber reinforced mortars. The detailed information of those specimens is shown in Table 2, where the numbers in the brackets of columns 4, 5 and 8 indicate the contents of the limestone, Glenium 151 and silica fume as percentages of the weight of cement, respectively. The amount of steel fiber is 0.3% by volume of the mortar. The specimens were identified with numbers designation: the first two numbers indicating water/binder ratio, the second two numbers corresponding to the content of silica fume, the last two numbers corresponding to the content of steel fiber. As an example, mortar 031003 implies a specimen with a water/binder ratio of 0.3, having 10% silica fume and 0.3 vol.% steel fiber.

2.2. Mixing and curing

The steel fiber reinforced mortars were mixed in a flat-bottomed mixer with a maximum volume of 12 l. The mixing procedure was as follows: 1) cementitious materials (including silica fume) and sands were blended for 1 min at lower speed; 2) following the next 4 min, half of the mixing water was firstly added during the mixing, then all the superplasticizer with the remaining water was added; then, the steel fibers were added in small batches to get a good dispersion of fibers in the mixes; 3) stop the mixing, substances sticking in the sides of the mixer were cleaned and mixed into the mixes within 1 min; 4) the mixture was allowed to rest for 5 min, then mixed for an additional 1 min at lower speed.

40×40×160 mm prisms were cast for nanoindentation test. During the casting, steel molds were vibrated in order to evacuate parts of the entrapped air. Then, surfaces of the specimens were carefully smoothed and covered with plastic sheets. Specimens were demolded after 24 h and were cured at 20 °C under water for 28 days.

Table 2
Characteristics of the mortar mixes.

Name	Mix proportion (kg/m^3)							
	Anlegg cement	Free water	Limestone	Glenium 151	Sand 0–4 mm	Sand 0–2 mm	Silica fume	Steel fiber
030003	543.0	153.7	47.2 (8.7%)	10.86 (2.0%)	1399.4	246.9	0.0 (0.0%)	24.2
031003	483.8	149.4	47.4 (9.8%)	12.10 (2.5%)	1399.4	246.9	48.4 (10.0%)	23.4
050003	411.5	201.5	47.3 (11.5%)	4.94 (1.2%)	1399.4	246.9	0.0 (0.0%)	23.4

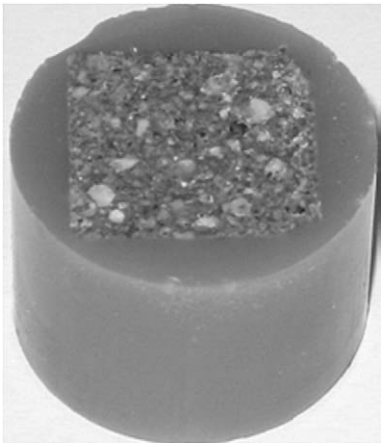

Fig. 1. Sample for grinding and polishing.

2.3. Sample preparation for nanoindentation test

Sample preparation is a very important step in the nanoindentation study since getting an extremely smooth surface is critical for the imaging and the reliable determination of local mechanical properties of the cement based composites [34]. Careful attention should be paid to the quality of the surface of the sample for the measurements of the elastic moduli and hardness by nanoindentation to ensure the reproducibility of the small penetration of the indenter [29]. It is suggested that a rough surface could increase scatter in the measured data by nanoindentation [39]. So far, polishing procedures for cement clinker [29] and hardened cement paste [32,34,40] have already been discussed in the literature. Although the microhardness in the fiber–matrix interface was studied [21] and nano-hardness in the fiber–paste interface was also reported [36], the detailed grinding and polishing procedures were hardly mentioned. Clearly, due to the differences in mechanical properties between steel fiber and mortar/concrete matrix, this will be an issue in practical experiments. The following procedure was therefore used.

After 28 days curing in a water bath, the central part of the $40\times40\times160$ mm prism was taken out by using a diamond saw. Later, this part was cut into small samples of the size about $15\times15\times15$ mm. Then, the $15\times15\times15$ mm samples were embedded in epoxy resin in air and the final samples prepared for grinding and polishing is shown in Fig. 1.

For fiber reinforced composites, due to the above mentioned lack of published grinding and polishing procedures, trial grinding and polishing procedures were made for several times. TegraForce-5 grinding and polishing machine, see Fig. 2, was used. At first, the SiC papers were used for the grinding and polishing. But the surface of the sample was convex when a straight edge was used to judge the surface flatness; also, the surfaces of steel fibers were full of scratches. Then, the MD-Piano plates (220, 600 and 1200) were selected for the coarse grinding to obtain flat surface. The Largo (9 μm), Dur (3 μm) and Dac (1 μm) were selected for the fine polishing to remove the scratches. The Nap was used for the final polishing. However, some surface fibers may be pushed out during the polishing procedures and the surfaces of the plates Dur and Dac were damaged. So, the force for each sample holder was varied. In addition, for samples with different water/binder ratio, the forces for each sample holder are also different due to different compressive strengths of the mortar. Good grinding and polishing procedures for samples with different water/binder ratio were finally determined, as shown in Table 3. At every step, a reflected light microscope was used to check the effectiveness of the grinding and polishing; and ultrasonic bath cleaning was performed to remove all dust and diamond particles. After the grinding and polishing, each sample was kept in a small air-tight container to prevent any dust resting on the test surface.

Fig. 2. Grinding and polishing machine.

Table 3
Grinding and polishing procedure for samples with different w/b.

Step	Name of the plate	Lubricant	Time (min)	Force for each sample holder (*N*)		Rotation speed (rpm)
				w/b = 0.3	w/b = 0.5	
1	MD-Piano 220	Water	2	30	15	150
2	MD-Piano 600	Water	1	20	15	150
3	MD-Piano 1200	Water	1	20	15	150
4	Largo	All/Largo (9 μm)	2	20	15	150
5	Dur	Dur (3 μm)	2	15	10	150
6	Dac	Wap-B (1 μm)	2	15	10	150
7	Nap	OP-U	2	15	10	150

Then, the surfaces of the polishing samples were studied by an AFM to obtain the topographic information. The surface roughness on 70 μm × 70 μm areas of steel fiber, aggregate, matrix and steel fiber–matrix interfacial zones was measured by using the EasyScan 2 AFM with *Z* resolution of 0.21 nm and *X*, *Y* resolution of 1.1 nm, and in tapping mode with the data being processed using the mean fit calculation.

2.4. Nanoindentation investigation

A Hysitron Triboindenter as shown in Fig. 3 [41] was used to determine the nano-mechanical properties. A common Berkovich indenter, i.e. a three-sided pyramidal diamond was used to study the fiber–matrix and fiber–matrix–aggregate interfacial zones. All testing was programmed in such a way that the indenter came into contact with the sample surface and the load increased at a constant rate of 1 mN/s until the load reached the maximum load of 5 mN. Then the load was held at its maximum for 2 s before unloading at the same constant rate. The protocol for the movement from one indent to the next was set as a Constant Direction Mode.

In the study of the ITZ, to avoid any statistical bias in the detection of microstructural features, the suggested minimum distance between two adjacent test points was 12.5 μm in the microhardness test of fiber reinforced cement paste [25]; while in the nanoindentation test on the fiber reinforced cementitious composite, the distance of indents was 5 μm in the direction perpendicular to the fiber and 8 μm in the parallel direction [36]. Since in the present test, it is difficult to determine the perpendicular and parallel directions of the steel fiber due to the random distribution of the fiber, the distance between two adjacent test points was set to be 10 μm or 11.4 μm. The intention was to spread a regular grid of points across the specific selected area of the sample. This large grid spacing also allows statistical analysis to be used to accurately determine the properties of the individual phases [33].

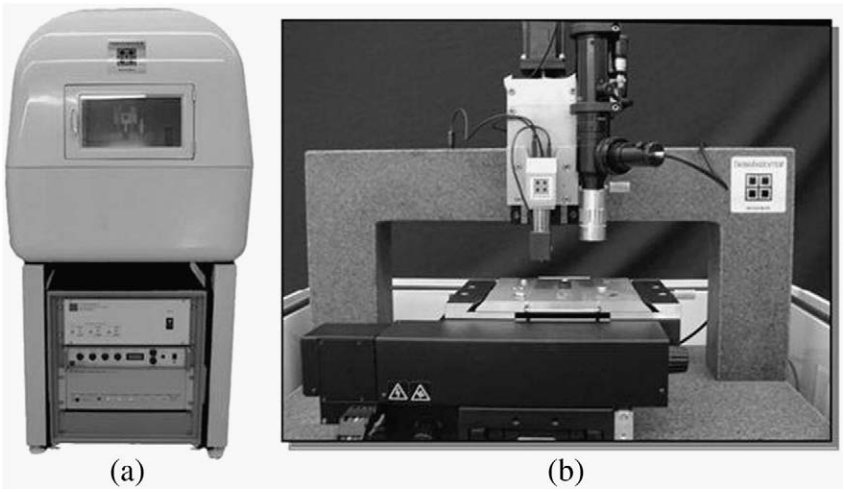

Fig. 3. Nanoindentation machine: (a) Triboindenter; (b) TriboScanner [41].

Nanoindentation consists of making contact between a sample and an indenter tip of known geometry and mechanical properties, followed by a continuously applied and recorded change in indentation load and indentation depth or displacement. A typical indentation load–depth curve is shown in Fig. 4a, where P_{max} is the peak indentation load; h_{max} is the indentation depth at the peak load; h_f is the final depth of the contact impression after unloading. For the penetration of an elastic half space by an axisymmetric indenter of arbitrary smooth profile, by applying a continuum scale model, the initial unloading stiffness $S = dP/dh$, given as follows [27]:

$$S = \frac{dP}{dh} = \frac{2}{\sqrt{\pi}} E_r \sqrt{A} \tag{1}$$

where A is the projected contact area at peak load. E_r is the reduced elastic modulus, given by:

$$\frac{1}{E_r} = \frac{\left(1-\nu^2\right)}{E} + \frac{\left(1-\nu_i^2\right)}{E_i} \tag{2}$$

where E and ν are Young's modulus and Poisson's ratio for the specimen and E_i and ν_i are the same parameters for the indenter. For the indenter used the present experiments, the elastic modulus $E_i = 1140$ GPa and the Poisson's ratio $\nu_i = 0.07$. Then, the elastic modulus E of the specimen can be calculated as follows:

$$E = \left(1-\nu^2\right) \cdot \left[\frac{1}{E_r} - \frac{\left(1-\nu_i^2\right)}{E_i}\right]^{-1} \tag{3}$$

If the Poisson's ratio ν for the specimen is given, the elastic modulus E for the specimen can be obtained. However, it is not easy to exactly determine this value for the steel fiber reinforced mortars prepared in this test. The suggested Poisson's ratio for mortar is $\nu = 0.2$ [42], this value is taken to calculate E in Eq. (3).

The hardness H, has the normal definition as follows:

$$H = \frac{P_{max}}{A} \tag{4}$$

Eqs. (1)–(4) have their origins in elastic contact theory. Later, the indentations of rigid indenter into an elastic-plastic half space have been experimentally conducted for different engineering materials [27,43]; and the finite element method has been used to study the material properties during elastic-plastic indentation to establish how the indentation process is influenced [44]. Now, this methodology is

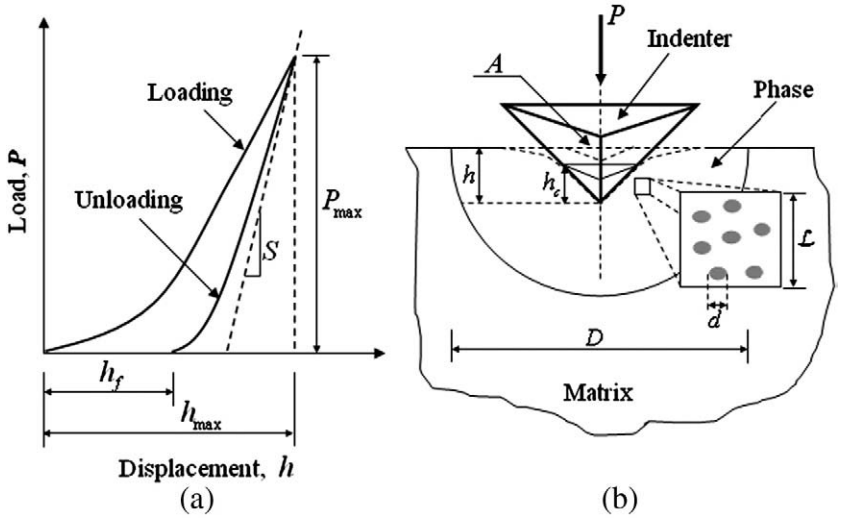

Fig. 4. (a) A typical representation of the indentation load versus indentation depth [27]; (b) Schematic representation of an indentation test with a Berkovich indenter on a homogeneous phase [44].

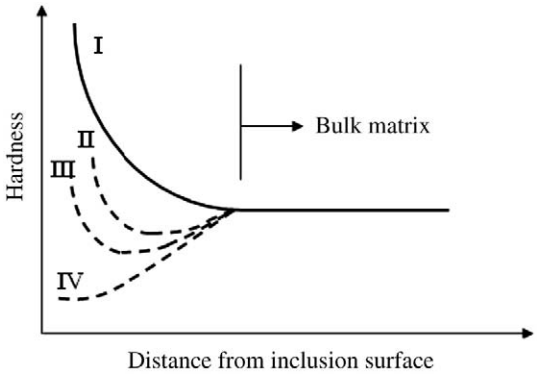

Fig. 5. Classification of microhardness profile in the interfacial transition zone (ITZ) around a rigid inclusion in a cement paste matrix [22].

widely used even for cementitious materials, such as cement paste, fiber reinforced composite and reinforced concrete [29–37], although heterogeneous features are exhibited in those cementitious composites.

To ensure that indentation results do not depend on any characteristic length, the scale separability condition must be verified for each phase [45]:

$$\frac{d}{10} \ll h_{\max} \ll \frac{D}{10} \tag{5}$$

where d and D stand for the characteristic sizes of the largest heterogeneity (particle size) and of the representative element volume, respectively (Fig. 4b). In other words, for $h_{\max}<d$ the indentation response will be affected by the heterogeneity dimension of the phase, and for larger depth $h_{\max}>D$ the indentation depth will be affected by the interaction of the different phases of the microstructure.

Actually, the characteristic size of the microstructure D in a particular phase is very difficult to estimate, as the microstructure itself

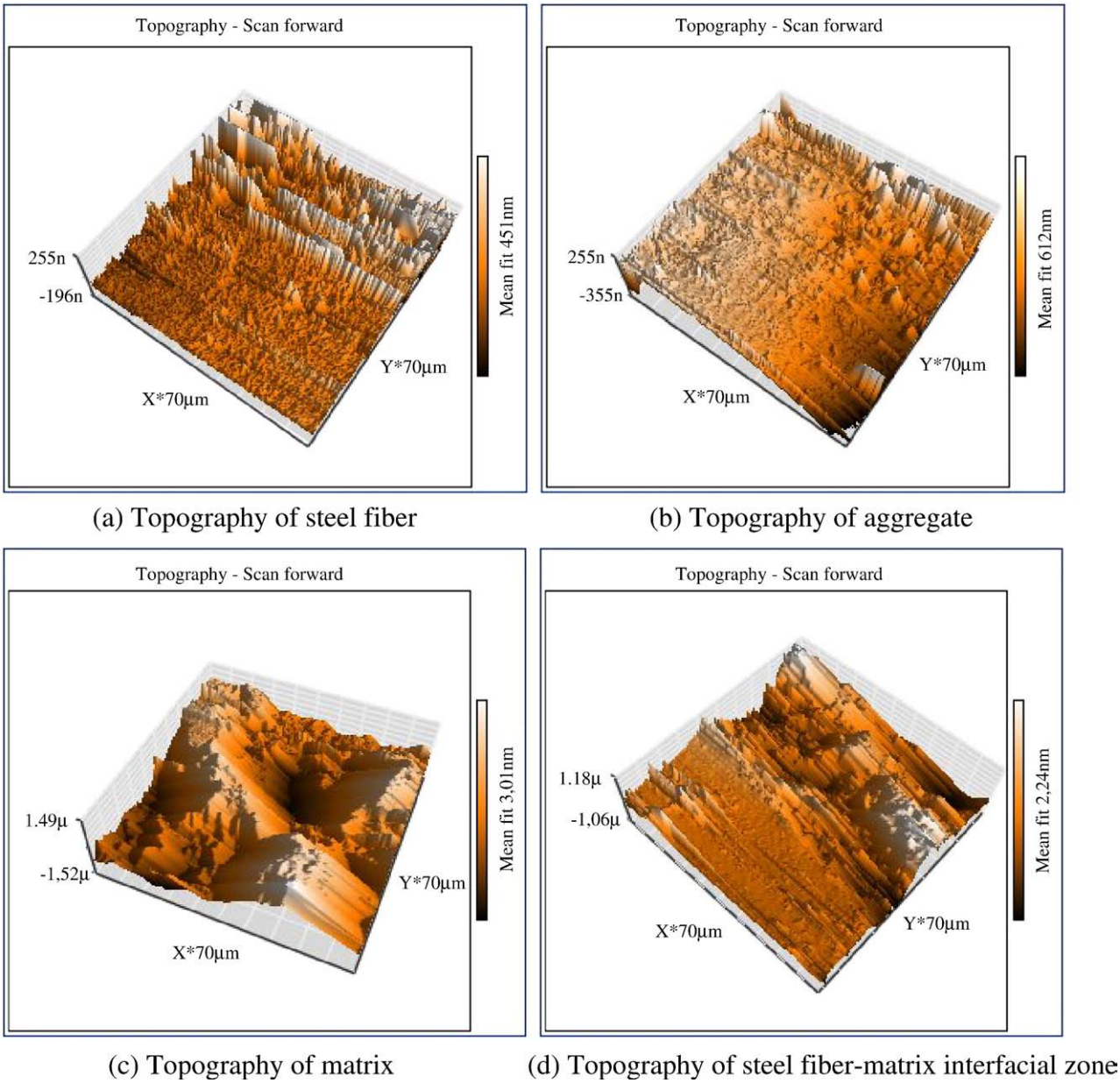

Fig. 6. Typical AFM topography image of the polished steel fiber reinforced mortar.

depends on mixing proportions, hydration degree, etc. Eq. (5) is only satisfied in an average sense, and that the presence of 'violators' of those conditions is inevitable, as pointed out by Constantinides and Ulm [35]. For a fully hydrated water/cement ratio of 0.5 cement paste, a good estimate of the characteristic length scale of the microstructure is on the order of D~1–3 μm, representing the smallest microstructural length scale among cement pastes' constituents (portlandite crystals and clinker particles are usually on the order of tens or hundreds of microns) [35]. Hence, based on the particle sizes of the materials shown in Table 1, the approximate characteristic length scale of the microstructure of the tested fiber reinforced mortar is estimated on the order of D~1–30 μm; and the range of maximum indentation depth is h_{max} [100,3000] nm.

2.5. SEM test

After the nanoindentation test, the microstructures of the interfaces were studied with Scanning Electron Microscopy (SEM). The sample surfaces were coated with carbon to increase the electrical conductivity of the sample. Secondary electron (SE) image and backscattered electron (BSE) image of the identical indented areas were obtained and the accelerating voltage was 15 kV for both SE imaging and BSE imaging.

2.6. Profiles characteristics of the ITZ

A variety of elastic modulus and microhardness or nanohardness profiles have been reported for the ITZ [6,15,21,36]. Common to all these test results is the observation that in the vicinity of the inclusion surface there is a gradient in the microhardness and elastic modulus, but in the bulk paste it becomes relatively constant. However, the nature of the microhardness gradients can be quite different. It was pointed out that the hardness in the ITZ should be smaller than that of the bulk due to the higher porosity of ITZ; on the other hand, such an observed reduction terminates as the inclusion surface is approached [6,21,36]. Rarely has a trend of consistently lower microhardness, right up to the inclusion surface, been reported [22]. The trends in the gradients can be classified into four types as shown in Fig. 5 [22]. The type I curve in Fig. 5 is expected to occur in systems in which (1) the matrix in the vicinity of the inclusion has the same properties as the bulk and the inclusion and the matrix are well bonded at the interface, or (2) the near surface ITZ is rich in massive CH [22]. Deviations from these conditions can lead to changes in the shape of the curve and can account for shapes such as II, III, and IV in Fig. 5.

3. Results and discussion

3.1. Effectiveness of the grinding and polishing procedures

The typical AFM topography image of the steel fiber, aggregate, matrix and steel fiber–matrix interfacial zones are shown in Fig. 6. Compared to the smaller height variation shown in steel fiber and aggregate, the larger height variation is observed in the matrix and ITZ. For the same sample, two or three locations were selected to study the surface roughness. The average roughness S_a, root-mean-square roughness S_q and peak-valley height S_y of the selected locations of the samples are summarized in Table 4. Due to the inherently heterogeneous of the polished surface resulting from the inherently heterogeneous of the mortar, the roughness measurements exhibit significant variability at various locations on the same sample.

The results show very smooth surfaces on the aggregate and steel fiber with the average roughness and root-mean-square roughness on the order of 10–65 nm, whereas the average roughness and root-mean-square roughness of matrix and steel fiber–matrix interfacial zone are found to be on the order of 120–475 nm. Compared to the small average roughness and root-mean-square roughness on the polished cement paste [35], those values of the matrix in our study are very high. The peak-valley height on aggregate and steel fiber is on the order of 320–1215 nm, while the peak-valley height on matrix is around 1.7 to 2.8 μm. On the interfacial zones of steel fiber–matrix, it is around 1.8 to 2.6 μm without a very clear gap. The peak-valley heights on matrix and ITZ probably reflect the porous nature of matrix and ITZ observed in the polished plane. Considering the 1.5 μm maximum height difference between different areas in the polished cement paste [38], the obtained maximum peak-valley height of aggregate and steel fiber, which is about 1.2 μm, is even better than that of the cement paste.

Table 4
Surface roughness measurement of the polished samples.

Name			Steel fiber	Aggregate	Matrix	Steel fiber–matrix interfacial zone
030003	Location 1	S_a (nm)				122.4
		S_q (nm)	–	–	–	178.4
		S_y (nm)				1835.4
	Location 2	S_a (nm)	48.4	26.0	146.1	
		S_q (nm)	63.5	37.4	197.4	–
		S_y (nm)	708.9	705.3	1747.8	
031003	Location 1	S_a (nm)	13.1	12.3	254.0	
		S_q (nm)	23.8	23.5	345.3	–
		S_y (nm)	524.9	531.0	2705.5	
	Location 2	S_a (nm)		26.7	160.8	234.6
		S_q (nm)	–	39.7	228.5	337.8
		S_y (nm)		430.6	2044.1	2569.0
050003	Location 1	S_a (nm)	12.6		385.4	216.6
		S_q (nm)	19.4	–	473.0	294.8
		S_y (nm)	329.0		2794.6	2420.1
	Location 2	S_a (nm)	15.4	21.0		
		S_q (nm)	27.1	35.8	–	–
		S_y (nm)	827.7	1190.8		
	Location 3	S_a (nm)	30.8	33.7	156.4	354.5
		S_q (nm)	58.4	48.2	228.6	438.1
		S_y (nm)	1146.0	1213.1	2288.6	2631.0

3.2. Data validation of the nanoindentation test

In order to determine the validity of each indentation, the P-h curves of each indented area were firstly checked. Typical P-h curves of steel fiber, aggregate and matrix are shown in Fig. 7a–c, respectively. Also, there are some discarded P-h curves, see Fig. 7d–f. Most of those irregular curves can be easily detected by their greater maximum indentation depths, as suggested by DeJong and Ulm [33]. The irregular nature of the curve shown in Fig. 7e may be due to the presence of a large void [38] while the discontinuous load–displacement curve shown in Fig. 7f may lie in the surface cracking during the force-driven indentation tests [33]. Due to the contact stiffness is measured only at peak load, and no restrictions are placed on the unloading data being linear during any portion of the unloading [27], curves showing nonlinear characteristic in the unloading portion are also adopted, see Fig. 7g.

Since eliminating discontinuous indentation curves and those in violation of the scale separability condition from the data set is of critical importance for accurate phase property identification [33], the scale separability condition Eq. (5) is also checked and curves in violation of Eq. (5) are eliminated. The resulting range of indentation depths of steel fiber, matrix and aggregate of the three samples are summarized in Table 5, where "Stdev" denotes the standard deviation of the indentation depth. It can be seen from Table 5 that the average indentation depths of steel fiber and aggregate are on the order of 160–210 nm, while the average indentation depth of matrix around 555–700 nm. Similar to the nanoindentation study of the fiber–matrix interface zone in the fiber reinforced ultra high performance concrete [45], the root-mean-square roughness of the polished samples shown

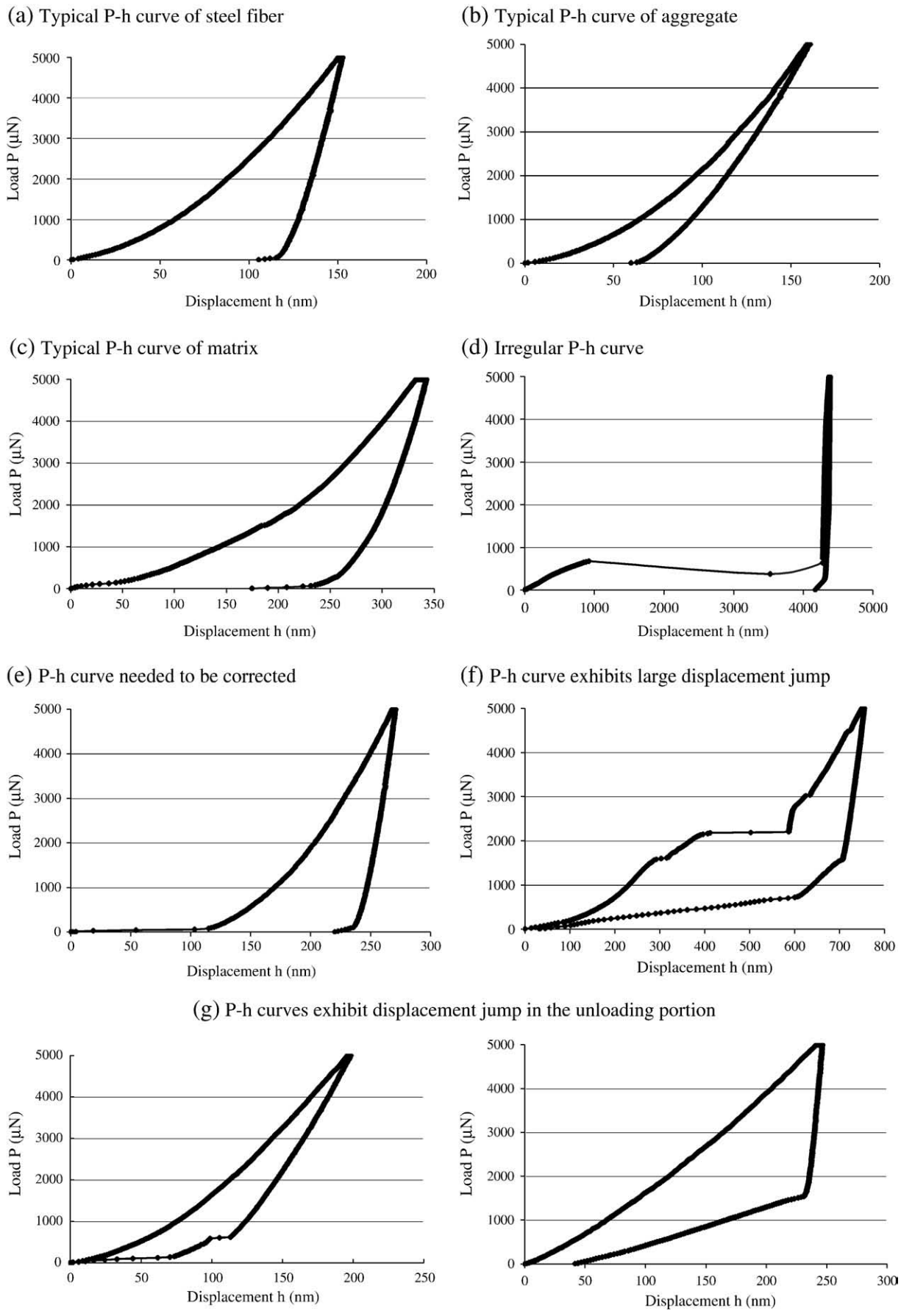

Fig. 7. Different characteristics of load–displacement (*P-h*) curves.

Table 5
Range of indentation depths of steel fiber, matrix and aggregate.

Name	h_{max} of steel fiber (nm)		h_{max} of matrix (nm)		h_{max} of aggregate (nm)	
	Mean	Stdev.	Mean	Stdev.	Mean	Stdev.
030003	162.4	5.3	555.3	290.5	204.8	17.8
031003	170.4	18.1	700.3	591.4	167.8	17.2
050003	162.8	5.6	650.3	313.5	187.3	15.4

Table 6
Percentage of discarded curves with "jump" or several "jumps" in each sample.

Name	Steel fiber–matrix interfacial zone	Steel fiber–matrix–aggregate interfacial zone
030003	3.8%	11.5%
031003	12.5%	9.1%
050003	13.6%	5.8%

in Table 4 indeed inferior to one order of magnitude of the average indentation depth, justifying the effectiveness of the present grinding and polishing procedures.

As pointed out by Constantinides and Ulm [35], the discontinuous load–displacement plots with a "jump" or several "jumps" in the indentation depth are related to surface preparation procedures, the largest percentage of discarded curves with "jump" or several "jumps" in each sample is checked. The number of curves excluded for this reason in each sample is shown in Table 6. It can be seen from Table 6 that the largest percentage of the three samples is smaller than 15%. Compared to the 5% percentage of discarded curves with "jump" or several "jumps" in cement paste [35], this number is quite high, indicating the further modification of the proposed grinding and polishing procedures.

As a result, due to the different mechanical properties among steel fiber, aggregate and matrix, sample preparation will be more difficult to handle in mortar and particularly in fiber reinforced mortar than in cement paste. Considering the more experience in preparation procedures for cement paste in nanoindentation tests [32,34,40], we conclude that our grinding and polishing procedures still yield a good overall surface roughness and will provide valuable information for the further study on the mechanical properties of ITZ in real materials, such as steel fiber reinforced concrete and reinforced concrete.

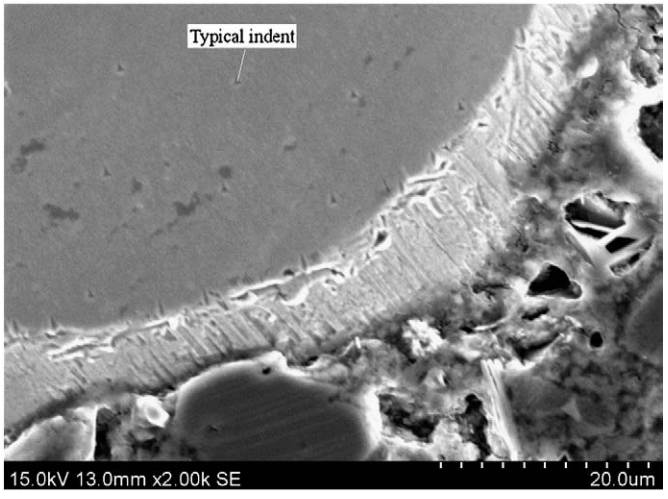

Fig. 8. SE image of indents made on the steel fiber.

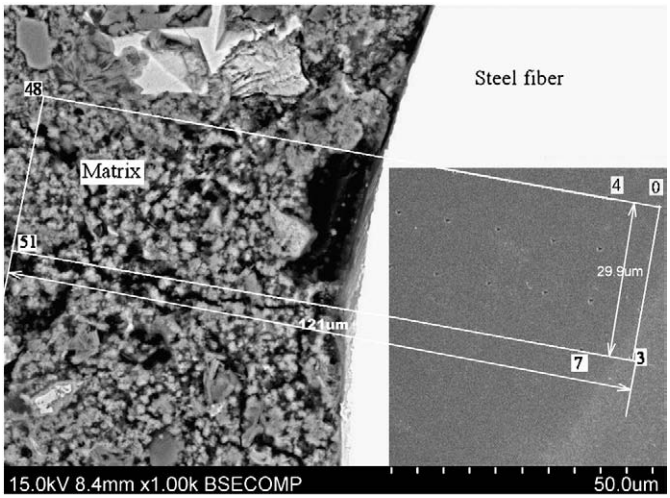

Fig. 9. Images of steel fiber–matrix interfacial zone in sample 030003, where the dimension of the indented area is 120 μm × 30 μm.

3.3. Nanoindentation and SEM test results

3.3.1. Steel fiber–matrix interfacial zone

After the data validation and calculation of the elastic moduli E of the sample of each indented area, the secondary electron (SE) image of each indented area was used to determine the distribution of all indents in each indented area. Actually, due to the very strong image contrast between the bright steel fiber and the dark matrix, only the distribution of the indents in the steel fiber can be found in the SE image of each indented area, see Fig. 8. In addition, the matrix exhibits very heterogeneous features. Unlike the cement paste samples used in most nanoindentation studies [29–35,38], it is difficult to find the indents in the matrix of steel fiber reinforced mortars. Thus, by using the distribution of the indents in the steel fiber in the SE image and the known dimension of the indented area, the whole size of each indented area in the SE image was determined; combined with the corresponding BSE image of the identical indented area, the interfacial bond conditions, the voids and microcracks within the indented area are observed. The whole indents were divided into appropriate groups: indents in the steel fiber, indents in the matrix, and/or indents in the aggregate. There are also indents in partially hydrated cement clinkers in some cases.

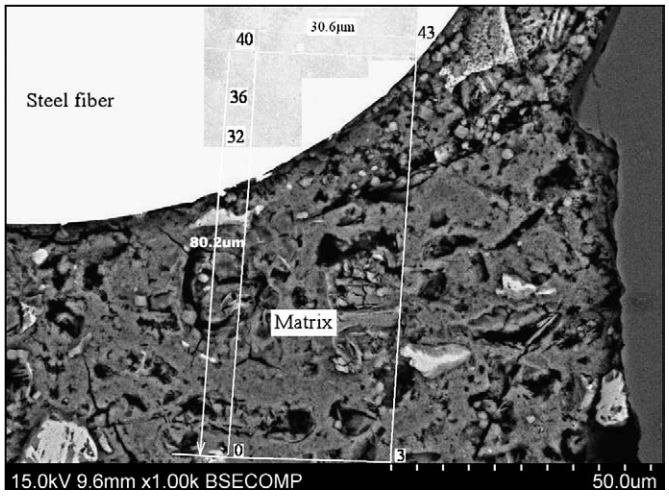

Fig. 10. Images of steel fiber–matrix interfacial zone in sample 031003, where the dimension of the indented area is 30 μm × 80 μm.

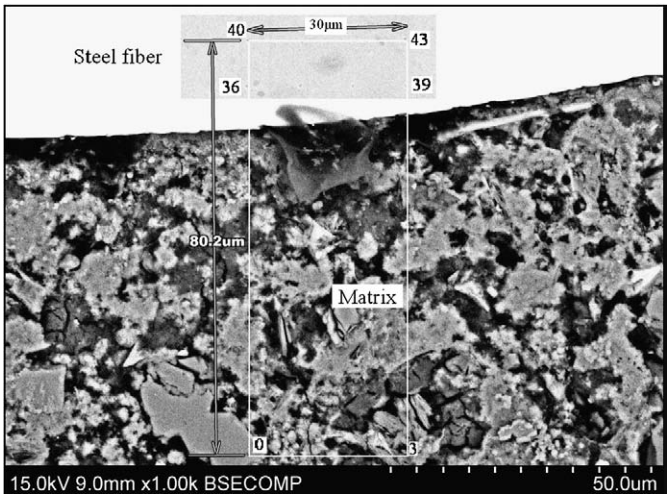

Fig. 11. Images of steel fiber–matrix interfacial zone in sample 050003, where the dimension of the indented area is 30 μm × 80 μm.

The size of each indented area in the SEM images of the steel fiber–matrix interfacial zones in samples 030003, 031003 and 050003 are shown in Figs. 9–11. The rectangular areas in Figs. 9–11 indicate the indented areas chosen for nanoindentation test, with 10 μm or 11.4 μm grid patterns as mentioned in Section 2; the numbers written in the image are the indented location, which always start from zero and also indicate the direction of the indenter movement in each chosen indented area. The elastic modulus and hardness profiles of the interfacial transition zone between steel fiber and matrix of the three samples are shown in Fig. 12, where the elastic modulus and hardness were determined as a function of the distance from the fiber surface and the vertical axis denotes the edge of the actual steel fiber.

In Fig. 12, there is a noticeable scatter within each sample; but an effort to discuss the features of the indentation profiles are made in the following section. For sample 030003, the hardness profile of the ITZ between steel fiber and matrix shows the trend of type I in Fig. 5. In the distance 5–35 μm from the steel fiber surface, there is an obvious increase in the hardness; the elastic modulus in this zone is also very high. Away from the surface of the steel fiber, i.e. in the 35–65 μm zones, the nano-mechanical properties become relatively constant and a plateau is reached. The hardness value at the weakest point is 0.1636 GPa, occurring approximately 56 μm away from the fiber surface. From the SEM image, see Fig. 9, it can be seen that the steel fiber and the matrix are well bonded at the interface, although there are still some defects such as a void, pores and discontinuous microcracks towards the edge of the steel fiber.

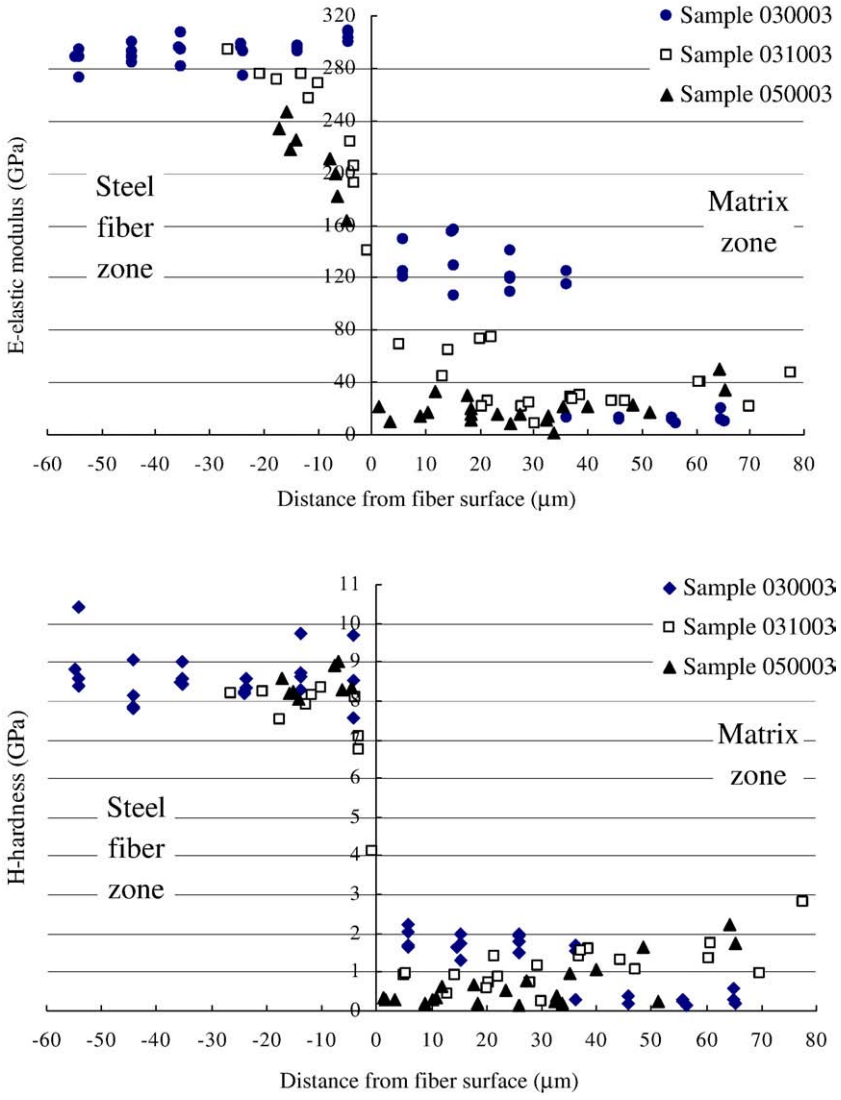

Fig. 12. Profiles of the steel fiber–matrix interfacial zone in samples 030003, 031003 and 050003.

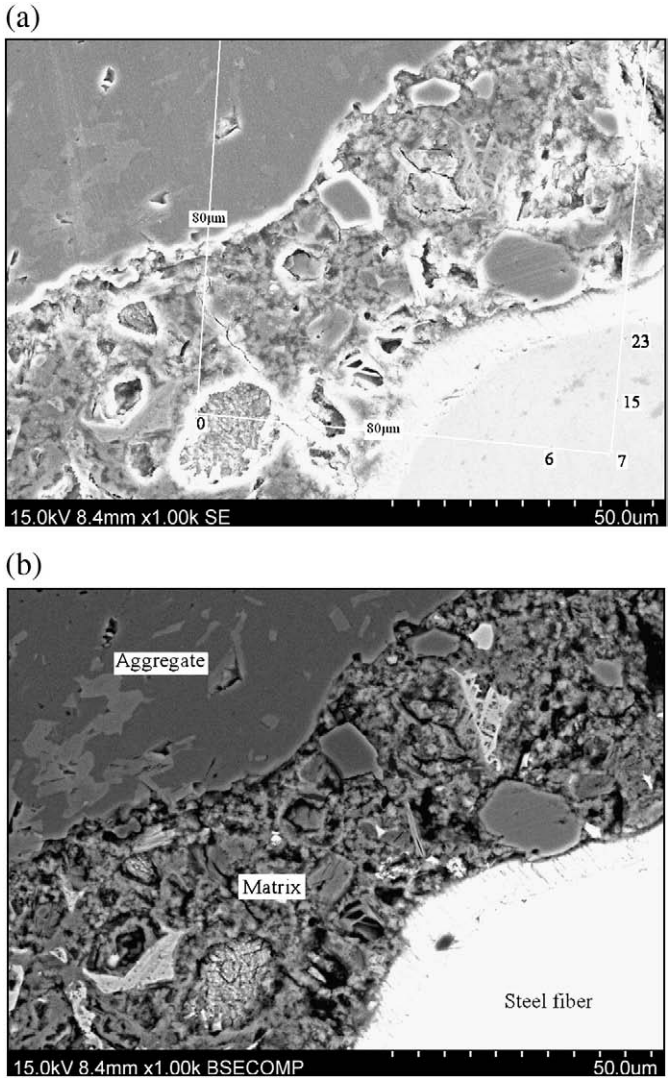

Fig. 13. Images of the steel fiber–matrix–aggregate interfacial zone in sample 030003: (a) SE image; (b) BSE image, where the dimension of the indented area is 80 μm × 80 μm.

For sample 031003, the whole hardness profile of the ITZ between steel fiber and matrix like type III in Fig. 5, but it is more uniform. Possibly due to the addition of the silica fume, the hardness profile of the ITZ is a bit different from that of sample 030003. It is interesting to note that there is no obvious trough in the interfacial zone; comparatively low hardness is observed just in the 10–30 μm zones and the nano-mechanical properties become relatively constant beyond this zone. The hardness value at the weakest point is 0.2391 GPa, occurring 30 μm away from the fiber surface, indicating an increase of the hardness at the weakest point owing to the 10% addition of the silica fume. Due to the high reactivity of the silica fume and the formation of compact CSH (calcium hydrosilicates) structures around the fibers [4], there seems to be more efficient bonding across the interface between the steel fiber and matrix in the SEM image (Fig. 10).

For sample 050003, the hardness profile of the ITZ shows a typical characteristic of type IV in Fig. 5. Comparing with the comparative high matrix hardness in samples 030003 and 031003, comparative low matrix hardness in mortar 050003 are observed due to the larger water/binder ratio, as pointed out by Sun et al. [21]. The lowest hardness is observed near the steel fiber surface, 25.6 μm away from the fiber surface. This value is 0.1452 GPa, indicating a decrease of the hardness at the weakest point due to the increase of the water/binder ratio. A trough is shown in the zones of 0–35 μm and relative constant properties are observed in the 35–65 μm zones. Those indicate that the interfacial bonding at the actual interface in sample 050003 is poor and not as effective as that obtained in samples with low water/binder ratio. The microstructure around the steel fiber is non-uniform, with discontinuous bleeding voids underneath the steel fiber, as shown in Fig. 11.

On the whole, in the samples with a low water/binder ratio of 0.3, the rise in the curves as the steel fiber surface is approached is observed, as reported by other researchers [6,21]. Although this rise in the curve as the inclusion surface is approached can be indicative of at least partial interfacial bonding at the interface that enables the inclusion to provide a re-straining effect on the indenter or the presence of massive CH, it may be at least partly due to an artifact [22]. For this reason, the curves shown in Fig. 12 are particularly beneficial when used for comparative purposes. It clearly indicates that, for a water/binder ratio of 0.3, the ITZ around steel fibers is not softer than the matrix; while for high water/binder ratio of 0.5, the ITZ around steel fibers is the weakest zone.

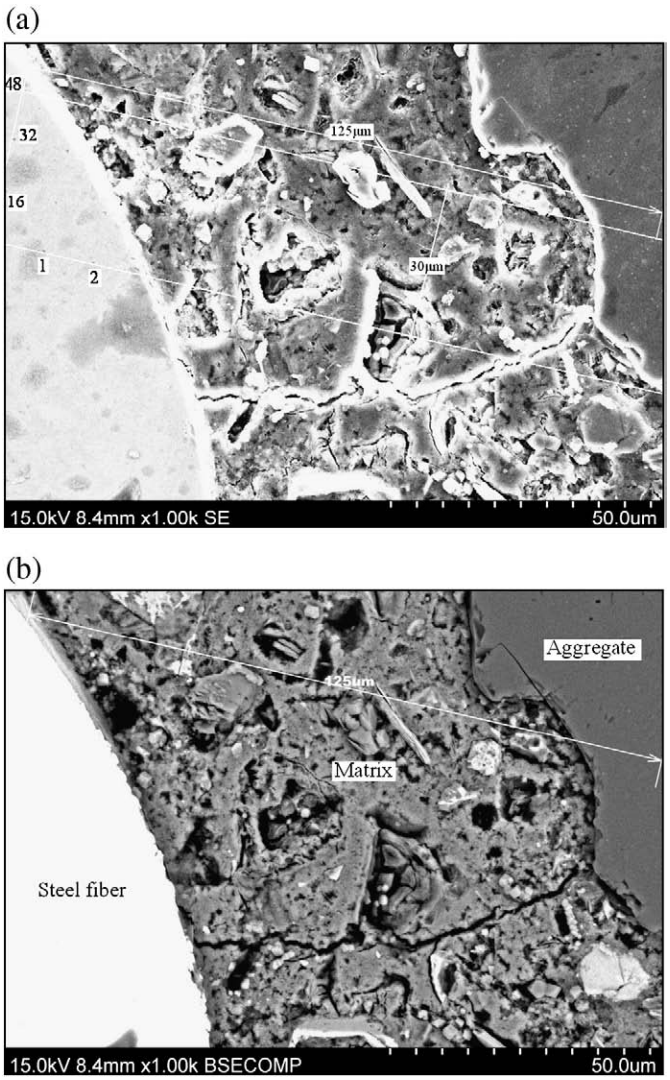

Fig. 14. Images of the steel fiber–matrix–aggregate interfacial zone in sample 031003: (a) SE image; (b) BSE image, where the dimension of the indented area is 150 μm × 30 μm.

In the experimental study of the ITZ between cement paste and aggregate [1,2], similar conclusions were also obtained. When the fine reactive silica fume is added to the mortar, the width of the ITZ between steel fiber and matrix is reduced and the interfacial bond is enhanced.

3.3.2. Steel fiber–matrix–aggregate interfacial zone

The size of each indented area in the SE image and the corresponding BSE image of the steel fiber–matrix–aggregate interfacial zones in samples 030003, 031003 and 050003 are shown in Figs. 13–15. The rectangular areas or part of the rectangular areas (due to the large indented area) indicate the indented areas; the numbers always start from zero and also indicate the direction of the indenter movement in each chosen indented area. From the SE image shown in Figs. 13a–15a, the indents in the steel fiber, indents in the matrix, indents in the aggregate and/or indents in partly hydrated cement can be easily determined. The elastic modulus and hardness profiles of the steel fiber–matrix–aggregate interfacial zones in three samples are shown in Figs. 16–18, where all the values were determined as a function of the distance from the fiber surface; the vertical axis denotes the edge of the actual steel fiber and the aggregate surface is schematically marked. It can be seen from Figs. 16–18 that the steel fiber has the highest elastic modulus while the aggregate has the highest hardness, indicating the initial differences among the different materials.

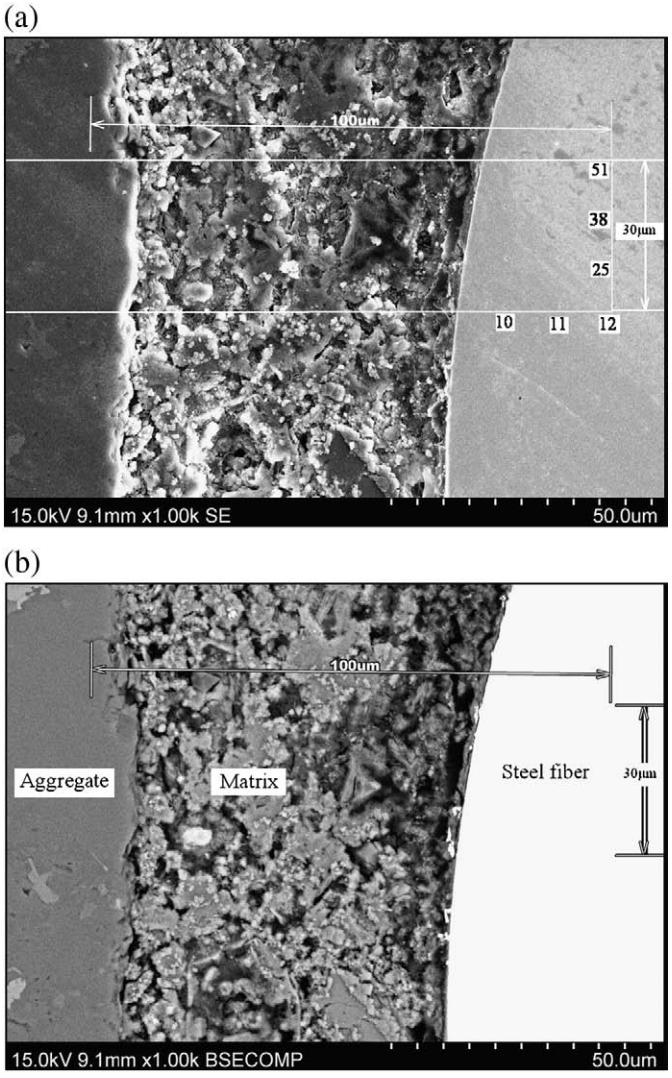

Fig. 15. Images of the steel fiber–matrix–aggregate interfacial zone in sample 050003: (a) SE image; (b) BSE image, where the dimension of the indented area is 120 μm × 30 μm.

In Fig. 16, the interfacial bond is efficient, as seen by the obvious rise in the hardness profile as the steel fiber and aggregate are approached. Low elastic modulus and hardness is observed in the distance of 20–40 μm away from the steel fiber surface. The hardness at the weakest point is 0.1859 GPa, occurring at an approximate distance of 50 μm away from the fiber surface. From the BSE image shown in Fig. 13b, ettringite needles can be seen in the approximate distance of 20 μm away from the steel fiber surface. Within this zone, there are also some partially hydrated cement clinkers near the aggregate and fiber surfaces, indicating not enough water to complete the hydration. Those clinkers may also attribute to the increase of elastic modulus near the surfaces. Since obvious rise in the curves as the steel fiber surface is approached is observed in steel fiber–matrix and steel fiber–matrix–aggregate zones, as shown in Figs. 12 and 16, it can be concluded that the bonding across the steel fiber interface is quite efficient in sample 030003.

In Fig. 17, the bonding across the steel fiber–matrix interface is good, as seen by the small rise in the hardness profile as the steel fiber is approached. However, this interfacial bond is not as efficient as that of the steel fiber–matrix interface shown in Fig. 16. In the distance of 20 to 80 μm away from the steel fiber surface, low elastic properties are exhibited. The hardness at the weakest point is very low, just 0.034 GPa. Cracking and voids may be the main reasons of these low mechanical properties and wide thickness of ITZ. With the approaching of the aggregate, rise in the profiles is observed. Considering the curves in Figs. 12 and 17, it can be concluded that the bonding across the steel fiber–matrix interface is good in 031003, but not as efficient as that in 030003. In addition, although the addition of silica fume results in no distinct presence of weak ITZ between steel fiber and matrix as shown in Fig. 12, in the steel fiber–matrix–aggregate interfacial zone, this effect is not obvious. From the BSE image shown in Fig. 14b, a void can be seen in the vicinity of the steel fiber. A large microcrack even extends from the steel fiber surface to the aggregate surface. After checking the picture of sample 031003, it is found that the aggregate in Fig. 14 has a very large size. This very large aggregate size may result in a more condensed microcrack in this narrow fiber–matrix–aggregate zone, as pointed out by Akçaoğlu et al. [9]. The autogenous shrinkage in the presence of comparatively large amounts of silica fume may also increase the microcracks [46].

In Fig. 18, a small increase in the hardness profile as the steel fiber is approached can be indicative of at least partial bonding at the interface. In the distance of 5–40 μm away from the steel fiber surface, low elastic properties are exhibited. The hardness at the weakest point is 0.1465 GPa, occurring near the fiber surface. It is very surprising to note that in the distance of 5–20 μm away from the aggregate surface, the elastic modulus and hardness are quite similar to those of the aggregate although it seems like part of the matrix from the BSE image shown in Fig. 15b. It is doubted that there maybe a piece of aggregate underneath this area. Considering the curves in Figs. 12 and 18, it can be concluded that there is only partial interfacial bonding at the steel fiber–matrix interface in sample 050003. Due to the discontinuous bleeding voids underneath the fiber (Fig. 11) and the obvious porous zone near the surface of the steel fiber (Fig. 15b), the fiber–matrix interfacial bond is not as good as that in sample 030003.

Considering the different thicknesses observed in the steel fiber–matrix and steel fiber–matrix–aggregate zones, it can be concluded that the thickness of the ITZ between steel fiber and matrix is on the order of 20 μm to 60 μm regardless of different matrix details, smaller than the suggested thickness [5]. As mentioned above, the largest thickness of the ITZ is observed in the narrow fiber–matrix–aggregate

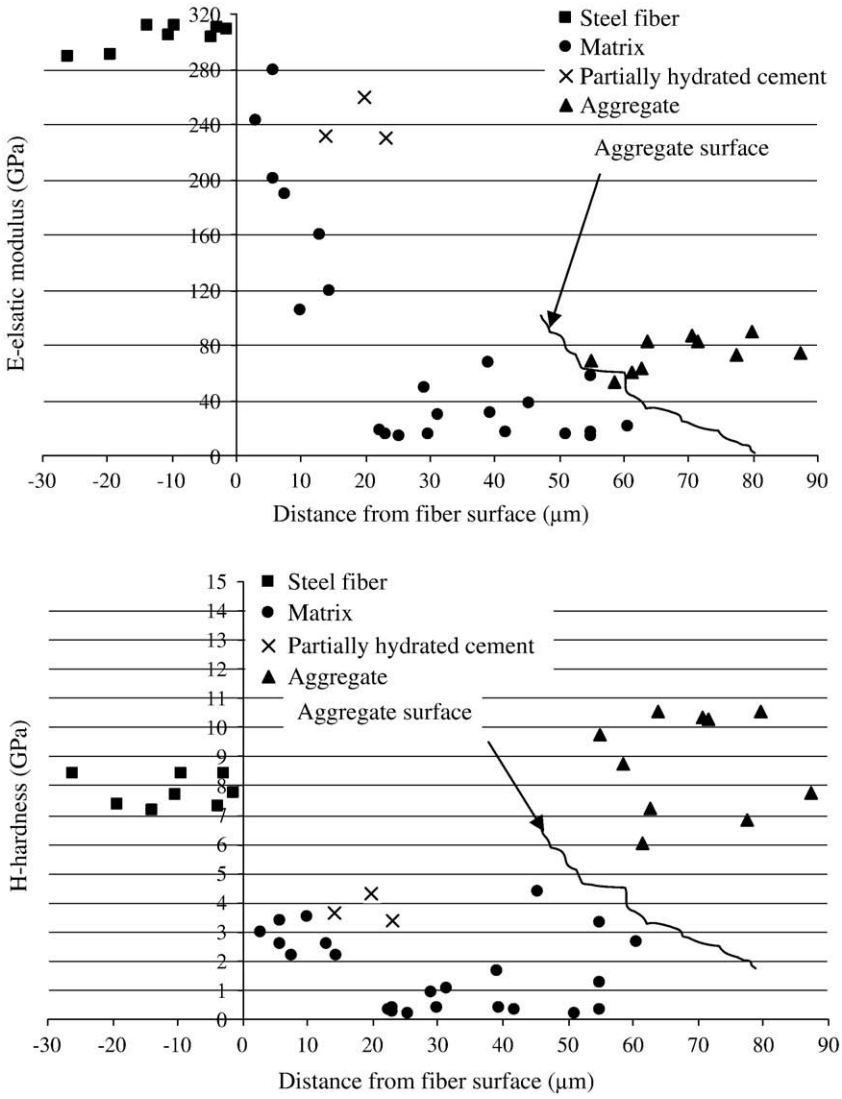

Fig. 16. Profiles of the steel fiber–matrix–aggregate interfacial zone in sample 030003.

zone in sample 031003, indicating the effect of aggregate size and different material shrinkage on the ITZ width.

It should be pointed out that, the choices of the number of the indented points in different materials and the distance between inclusion surface and matrix are very crucial for the profiles of the ITZ. For instance, in the selected steel fiber–matrix zone in sample 030003, there are no indented points located at the edge of the steel fiber, see Fig. 9. The nearest indented column is about 4 μm away the actual fiber surface, resulting in an obvious discontinuous jump the in the profiles of the ITZ in this sample. On the other hand, the profiles of the steel fiber–matrix interfacial zones in the other two samples are quite continuous, indicating a better choice of the indented points. The similar discontinuous jump near the aggregate surface is also observed in Fig. 18.

4. Conclusions

Steel fiber reinforced mortars were prepared to study the steel fiber–matrix and fiber–matrix–aggregate interfaces, where water/binder ratios of 0.3 and 0.5 were used as well as two different contents of silica fume (0% and 10%) were considered. The characteristics of the profiles of the elastic modulus and nanoindentation hardness of the interfacial transition zones have been analyzed. This research work has led to the following conclusions:

1) Sample preparation is very critical for nano-scale characterization. Due to the lack of published grinding and polishing procedures for steel fiber reinforced composites in literature, several trial procedures were made. Final grinding and polishing procedures were determined and AFM surface measurements of the polished samples were carried out to check the effectiveness of the proposed grinding and polishing procedures. The AFM study and nanoindentation tests show that the grinding and polishing procedures yield a good overall surface roughness and robust nanoindentation results.
2) For samples with different water/binder ratios, the characteristics of the profiles of the elastic modulus and nanoindentation hardness of the interfacial transition zones are quite different. In sample 030003, efficient bonding across the steel fiber–matrix and fiber–matrix–aggregate interfaces is shown as increased hardness profile as steel fiber and aggregate are approached. For samples with large water/binder ratio, i.e. sample 050003, due to the discontinuous bleeding voids underneath the fiber, the fiber–matrix bond is not very good. Just a small rise in the hardness

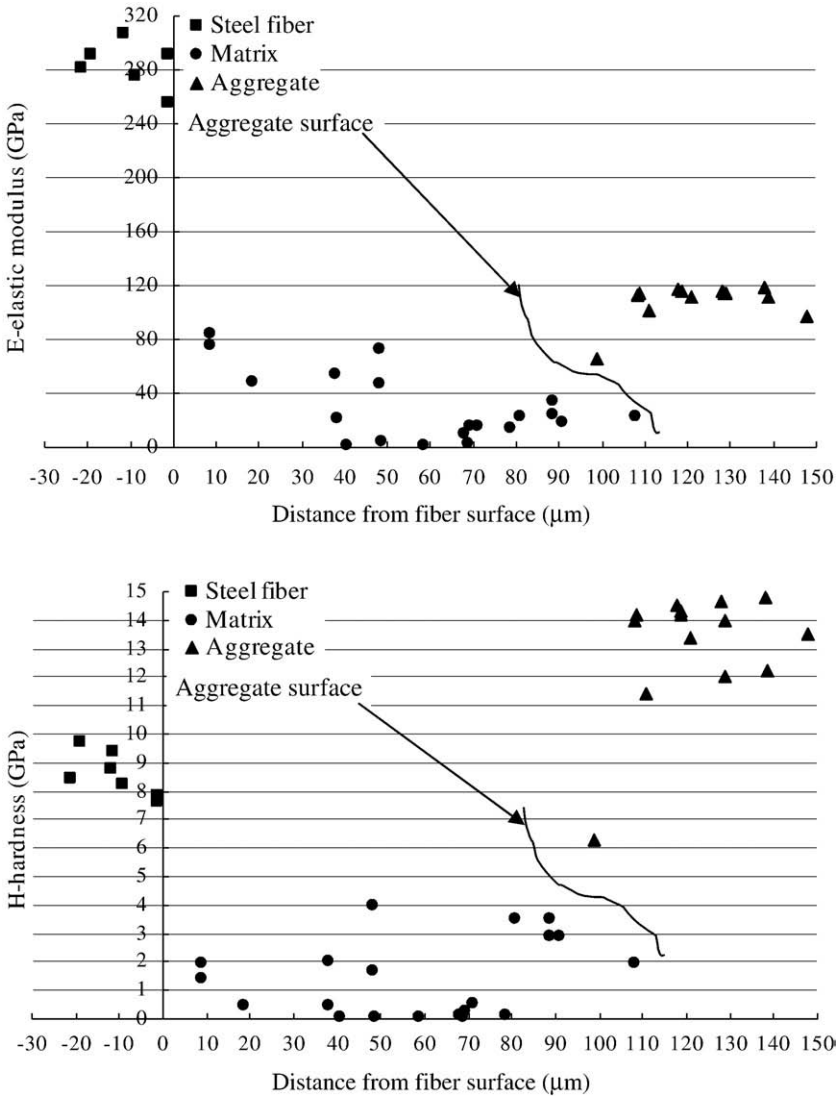

Fig. 17. Profiles of the steel fiber–matrix–aggregate interfacial zone in sample 031003.

profile as the steel fiber is approached can be observed in the steel fiber–matrix–aggregate interface; while obvious trough is shown in the steel fiber–matrix interface. In addition, the hardness value at the weakest point in the transition zone in sample 050003 is smaller than that in 030003, indicating the effect of the water/binder ratio on the ITZ quality.

3) The characteristics of the profiles of the elastic modulus and nanoindentation hardness of the interfacial transition zones are also influenced by the addition of silica fume. In sample 031003 with 10% silica fume, when the steel fiber and aggregate are approached, rise in the hardness profile is observed, indicating good interfacial bonding across those transition zones. However, the bonding across the steel fiber–matrix interface is not as efficient as that of the steel fiber–matrix interface in sample 030003 without silica fume, since the rise in the hardness profile is comparatively low and void is presented in the vicinity of steel fiber. In some parts of the sample, the addition of silica fume leads to no distinct presence of weak ITZ in the steel fiber–matrix transition zone and the interfacial bond condition is efficient; while in other parts of the sample, such as the steel fiber–matrix–aggregate interfacial zone, the effect of the silica fume is not obvious. In addition to the inherent variation of the individual constituents composing fiber reinforced mortars, such as the variable aggregate size, the differential shrinkage of the two materials, it is suggested that air content should be carefully controlled to decrease voids in interfacial transition zones of the sample.

This experimental work helps to understand the nano-mechanical properties of steel fiber–matrix and fiber–matrix–aggregate interfaces in the steel fiber reinforced composites. Those nano-mechanical properties will influence and determine the macroscopic mechanical properties of fiber reinforced cement based materials. Linking the nano-mechanical properties of the ITZ with the macroscopic mechanical properties will help to proceed in the development of more ductile cement based materials.

Acknowledgements

This research was done at the Norwegian University of Science and Technology (NTNU), when the first author is working at the Department of Structural Engineering as a visiting professor for one year. The first author gratefully thanks the support by the Norwegian Research Councils a part of the Cultural Agreement between Norway and China—Government scholarships 2007/2008 (No. 26X35003) and the National Natural Science Foundation of China (No. 50508020).

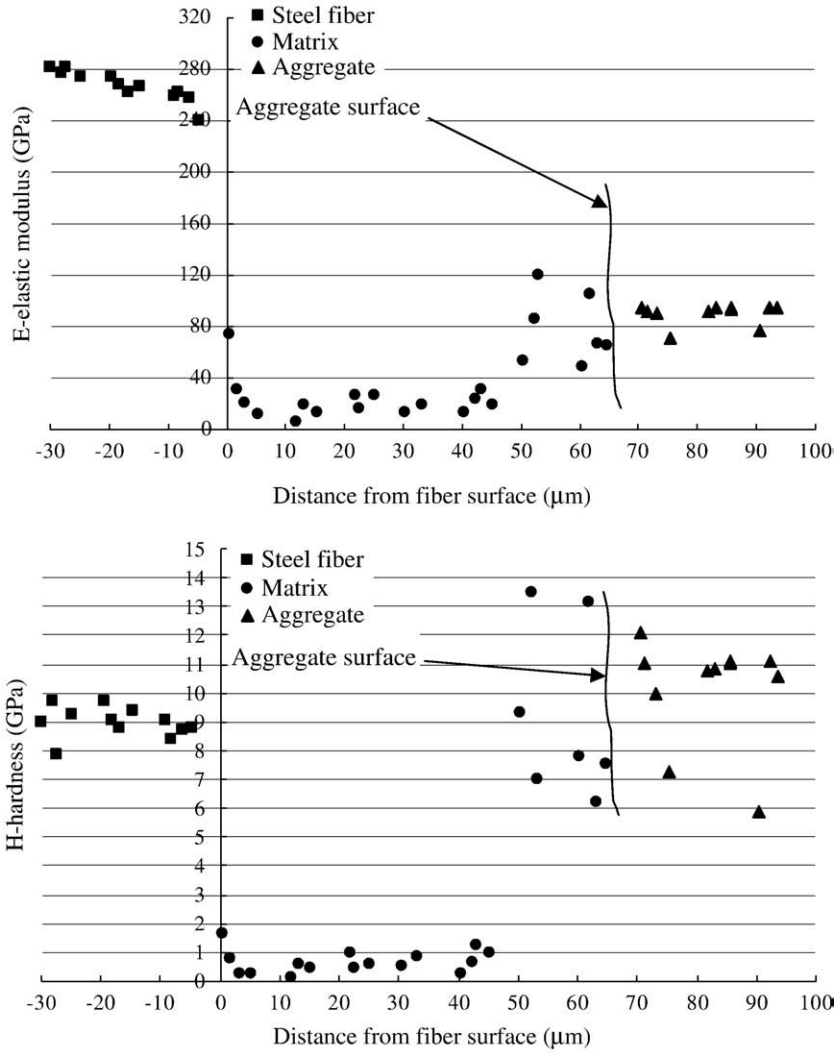

Fig. 18. Profiles of the steel fiber–matrix–aggregate interfacial zone in sample 050003.

The invitation provided by Professor Stefan Jacobsen in NTNU to cooperate with this research work is gratefully appreciated. In addition, the financial support from the COIN (Concrete Innovation Centre) Project 3–3.5—Nanotechnology applied to Cement-based Materials is greatly appreciated. Help given by engineer Ove Edvard Loraas, engineer Arild Monsøy and Wilhelm Dall in NTNU is also acknowledged.

References

[1] R. Zimbelmann, A contribution to the problem of cement-aggregate bond, Cem. Concr. Res. 15 (5) (1985) 801–808.
[2] K.L. Scrivener, A.K. Crumbie, P. Laugesen, The interfacial transition zone (ITZ) between cement paste and aggregate in concrete, Interface Sci. 12 (4) (2004) 411–421.
[3] J.P. Ollivier, J.C. Maso, B. Bourdette, Interfacial transition zone in concrete, Adv. Cem. Based Mater. 2 (1) (1995) 30–38.
[4] C. Redon, J.-L. Chermant, Compactness of the cement microstructure versus crack bridging in mortars reinforced with amorphous cast iron fibers and silica fumes, Appl. Compos. Mater. 8 (3) (2001) 149–161.
[5] V.C. Li, H. Stang, Interface property characterization and strengthening mechanisms in fiber reinforced cement based composites, Adv. Cem. Based Mater. 6 (1) (1997) 1–20.
[6] W. Zhu, P.J.M. Bartos, Application of depth-sensing microindentation testing to study of interfacial transition zone in reinforced concrete, Cem. Concr. Res. 30 (8) (2000) 1299–1304.
[7] A. Bentur, M.G. Alexander, D. Bentz, O. Buyukozturk, J. Elsen, D. Hooton, H. Jennings, A. Katzs, K.O. Kjellsen, A. Kronlof, B. Laggerblad, S. Mindess, J.-P. Ollivier, K. Scrivener, J. Skalny, et al., Review of the work of the RILEM TC 159-ETC: Engineering of the interfacial transition zone in cementitious composites, Mat. Struct. 33 (2) (2000) 82–87.
[8] A.U. Nilsen, P.J. Monteiro, Concrete: a three phase material, Cem. Concr. Res. 23 (1) (1993) 147–151.
[9] T. Akçaoğlu, M. Tokyay, T. Çelik, Effect of coarse aggregate size and matrix quality on ITZ and failure behavior of concrete under uniaxial compression, Cem. Concr. Compos. 26 (6) (2004) 633–638.
[10] T. Akçaoğlu, M. Tokyay, T. Çelik, Assessing the ITZ microcracking via scanning electron microscope and its effect on the failure behavior of concrete, Cem. Concr. Res. 35 (2) (2005) 358–363.
[11] S. Diamond, J. Huang, The ITZ in concrete – a different view based on image analysis and SEM observations, Cem. Concr. Compos. 23 (2–3) (April 2001) 179–188.
[12] J. Hu, P. Stroeven, Properties of the interfacial transition zone in model concrete, Interface Sci. 12 (4) (2004) 389–397.
[13] Y.-W. Chan, V.C. Li, Effects of transition zone densification on fiber/cement paste bond strength improvement, Adv. Cem. Based Mater. 5 (1) (1997) 8–17.
[14] Y.-W. Chan, V.C. Li, Age effect on the characteristics of fibre/cement interfacial properties, J. Mater. Sci. 32 (19) (1997) 5287–5292.
[15] S. Igarashi, A. Bentur, S. Mindess, Effect of processing on the bond and interfaces in steel fiber reinforced cement composites, Cem. Concr. Compos. 18 (5) (1996) 313–322.
[16] Y.-W. Chan, S.-H. Chu, Effect of silica fume on steel fiber bond characteristics in reactive powder concrete, Cem. Concr. Res. 34 (7) (2004) 1167–1172.
[17] O. Kayali, Effect of high volume fly ash on mechanical properties of fiber reinforced concrete, Mat. Struct. 37 (5) (2004) 318–327.
[18] L. Gatty, S. Bonnamy, A. Feylessoufi, C. Clinard, P. Richard, H. Van Damme, A transmission electron microscopy study of interfaces and matrix homogeneity in ultra-high-performance cement-based materials, J. Mater. Sci. 36 (16) (2001) 4013–4026.

[19] K.L. Scrivener, Backscattered electron imaging of cementitious microstructures: understanding and quantification, Cem. Concr. Compos. 26 (8) (2004) 935–945.
[20] A.R. Brough, A. Atkinson, Automated identification of the aggregate-paste interfacial transition zone in mortars of silica sand with Portland or alkali-activated slag cement paste, Cem. Concr. Res. 30 (6) (2000) 849–854.
[21] W. Sun, J.A. Mandel, S. Said, Study of the interface strength in steel fiber-reinforced cement-based composites, J. Am. Concr. Inst. 83 (4) (1986) 597–605.
[22] S. Igarashi, A. Bentur, S. Mindess, Microhardness testing of cementitious materials, Adv. Cem. Based Mater. 4 (2) (1996) 48–57.
[23] W. Zhu, P.J.M. Bartos, Assessment of interfacial microstructure and bond properties in aged GRC using a novel microindentation method, Cem. Concr. Res. 27 (11) (1997) 1701–1711.
[24] P. Trtik, P.J.M. Bartos, Micromechanical properties of cementitious composites, Mat. Struct. 32 (5) (1999) 388–393.
[25] W.M. Cross, K.H. Sabnis, L. Kjerengtroen, J.J. Kellar, Microhardness testing of fiber-reinforced cement paste, ACI Mater. J. 97 (2) (2000) 162–167.
[26] K. Velez, F. Sorrentino, Characterization of cementitious materials by nanoindentation, in: W. Kurdowski, M. Gawlicki (Eds.), Kurdowski Symposium—Science of Cement and Concrete, Krakow, June 20–21, 2001, pp. 67–77.
[27] W.C. Oliver, G.M. Pharr, Improved technique for determining hardness and elastic modulus using load and displacement sensing indentation experiments, J. Mater. Res. 7 (6) (1992) 1564–1580.
[28] G. Constantinides, F.-J. Ulm, K. Van Vliet, On the use of nanoindentation for cementitious materials, Mat. Struct. 36 (3) (2003) 191–196.
[29] K. Velez, S. Maximiliena, D. Damidotb, G. Fantozzia, F. Sorrentinob, Determination by nanoindentation of elastic modulus and hardness of pure constituents of Portland cement clinker, Cem. Concr. Res. 31 (4) (2001) 555–561.
[30] G. Constantinides, F.-J. Ulm, The effect of two types of C–S–H on the elasticity of cement-based materials: results from nanoindentation and micromechanical modeling, Cem. Concr. Res. 34 (1) (2004) 67–80.
[31] H.M. Jennings, J.J. Thomas, J.S. Gevrenov, G. Constantinides, F.-J. Ulm, A multi-technique investigation of the nanoporosity of cement paste, Cem. Concr. Res. 37 (3) (2007) 329–336.
[32] W. Zhu, J.J. Hughes, N. Bicanic, C.J. Pearce, Nanoindentation mapping of mechanical properties of cement paste and natural rocks, Mater. Charact. 58 (11–12) (2007) 1189–1198.
[33] M.J. DeJong, F.-J. Ulm, The nanogranular behavior of C–S–H at elevated temperatures (up to 700 °C), Cem. Concr. Res. 37 (1) (2007) 1–12.
[34] P. Mondal, S.P. Shah, L. Marks, A reliable technique to determine the local mechanical properties at the nanoscale for cementitious materials, Cem. Concr. Res. 37 (10) (2007) 1440–1444.
[35] G. Constantinides, F.-J. Ulm, The nanogranular nature of C–S–H, J. Mech. Phys. Solids 55 (1) (2007) 64–90.
[36] J. N meček, P. Kabele, Z. Bittnar, Nanoindentation based assessment of micro-mechanical properties of fiber reinforced cementitious composite, 6th RILEM Symposium on Fiber-Reinforced Concrete (FRC)- BEFIB, 2004, Varenna, Italy, 2004, pp. 401–410.
[37] W. Zhu, M. Sonebi, P.J.M. Bartos, Bond and interfacial properties of reinforcement in self-compacting concrete, Mat. Struct. 37 (7) (2004) 442–448.
[38] P. Mondal, S.P. Shah, L.D. Marks, Nanoscale characterization of cementitious materials, ACI Mater. J. 105 (2) (2008) 174–179.
[39] J.Y. Kim, J.J. Lee, Y.H. Lee, J. Jang, D. Kwon, Surface roughness effect in instrumented indentation: a simple contact depth model and its verification, J. Mater. Res. 21 (12) (2006) 2975–2978.
[40] M. Miller, C. Bobko, M. Vandamme, F.-J. Ulm, Surface roughness criteria for cement paste nanoindentation, Cem. Concr. Res. 38 (4) (2008) 467–476.
[41] TriboIndenter User Manual, Hysitron Inc., Minneapolis, MN, 2005.
[42] K.M. Lee, J.H. Park, A numerical model for elastic modulus of concrete considering interfacial transition zone, Cem. Concr. Res. 38 (3) (2008) 396–402.
[43] M. Sakai, Y. Nakano, Elastoplastic load–depth hysteresis in pyramidal indentation, J. Mater. Res. 17 (8) (2002) 2161–2173.
[44] G.M. Pharr, A. Bolshakov, Understanding nanoindentation unloading curves, J. Mater. Res. 17 (10) (2002) 2660–2671.
[45] L. Sorelli, G. Constantinides, F.-J. Ulm, F. Toutlemonde, The nano-mechanical signature of ultra high performance concrete by statistical nanoindentation techniques, Cem. Concr. Res. 38 (12) (2008) 1447–1456.
[46] R.F. Feldman, C. Huang, Properties of Portland cement-silicate fume pastes – porosity and surface properties, Cem. Concr. Res. 15 (5) (1985) 765–774.